The application of a Local Dimensionality Estimator to the analysis of 3-D microscopic network structures

Geert M.P. van Kempen[1], Niels van den Brink[2], Lucas J. van Vliet[2], Michael van Ginkel[2], Piet W. Verbeek[2] and Han Blonk[1]

[1]Unilever Research Vlaardingen, Olivier van Noortlaan 120, 3133 AT Vlaardingen, The Netherlands
[2]Pattern Recognition Group of the Department of Applied Physics, Delft University of Technology
Lorentzweg 1, 2628 CJ Delft, The Netherlands

e-mail: {Geert-van.Kempen, Han.Blonk}@Unilever.com, {lucas, michael, piet}@ph.tn.tudelft.nl

Abstract

We present the application of a local dimensionality estimator to the analysis of 3-D microscopic network structures. Three-dimensional images of these structures have been acquired with a fluorescence confocal microscope. We derive the smoothed gradient square tensor (GST) in 3D and show how the eigenvalues and eigenvectors of the tensor can be computed analytically. The eigenvalues yield the dimensionality, the eigenvectors the corresponding orientation. The application of the GST to analyse isotropic, cylindrical and planar structures is tested on synthetic data. The GST analysis of the confocal data requires a reliable measurement of the fluorescence intensities as well as a adequate resolution. We shown that an optimisation of the fluorescence staining combined with an attenuation correction guarantees the former, whereas image restoration will deliver the latter. Finally, results of the application of the GST to confocal data are presented.

1. Introduction

Health-conscious consumers have created a tremendous demand for low-fat products. Reducing the amount of fat in a product can be quite a challenge. Margarine, which is the main subject of this research, normally consists of approximately 80% fat and the remaining part is primarily water. Water is cheaper and more common than fat and therefore would be an ideal fat-replacement. For halvarine the fat concentration has already been reduced to 40%, or even 20% for low-fat margarine. The process of producing low-fat foods is not simply one of taking out fat however. The fat molecules form a network that gives margarine its characteristic structure and determines important properties such as taste, mouthfeel and strength of the margarine. If we reduce the fat-contents too much, the fat-structure is not strong enough to contain the water and we get a liquid state (Figure 1). In order to create low-fat spreads (< 5% fat) another way to structure the water is needed.

The water can be structured using a liquid-crystalline phase [1]. The liquid-crystalline phase is created under the influence of surface-active substances. An example of a surface-active substance is a molecule with a hydrophilic head and a hydrophobic tail.

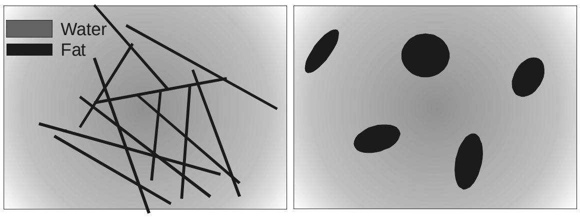

Figure 1: Structuring of water using fat. On the left margarine (> 20% fat) and on the right a low-fat spread (< 5% fat)

For the structuring of water it is most interesting when both the head and the tail are about equally sized (Figure 2.a). The molecules then form themselves in a so-called bi-layered structure with the tails close to each other (Figure 2.b). On a local scope the heads and tails of the molecules are very mobile, just like in a liquid. There is a larger scale ordering present though, giving the substance many properties of a crystal. Many surface-active substances, e.g. monoglycerides, form this bi-layered structure. Monoglycerides have been used for a number of years in a wide variety of food products [1].

In three dimensions the bi-layered structures form a lamellar phase. By cooling the lamellar phase the tails of the surface-active molecules lose their liquid character and become more rigid. The water/monoglyceride mixture enters the α-gel phase, which is much more consistent. This phase is thermodynamically not stable and will convert to a phase that is called the coagel phase [1]. The coagel phase is not quite a structure of layers, but more a network or matrix of planar crystals (Figure 2.c). This network is quite comparable to the network fat forms while containing oil.

Geert M.P. van Kempen, Niels van den Brink, Lucas J. van Vliet, Michael van Ginkel, Piet W. Verbeek and Han Blonk, *"The application of a Local Dimensionality Estimator to the analysis of 3-D microscopic network structures"*, in the proceedings of the 11th Scandinavian Conference on Image Analysis, Kangerlussuaq, Greenland, june 7-11, 1999, pp. 447-455

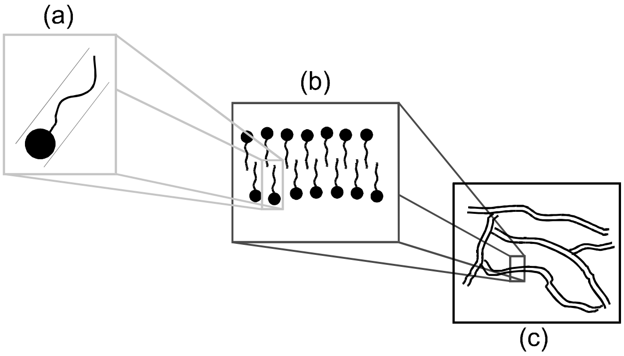

Figure 2: Surface-active substance with a hydrophobic tail as wide as its hydrophilic head.

The microstructure of fat has well-known rheological properties. Those of the water-structuring monoglyceride are less well known. To study and understand waterstructuring we need quantitative measures to characterise these microstructures. In this paper we focus on estimation of the local dimensionality of the matrix.
In section 2 we derive a closed-form expression for the eigenvalues and eigenvectors of the 3-D Gradient Square Tensor (GST). In section 3 we present tools for the determination of the local dimensionality based on the GST. Results performed on synthetic data are presented in section 4. Section 5 discusses the optimization of confocal imaging for quantitative image analysis and presents an application of the GST to the analysis of microscopic network structures. In section 6 these results will be discussed and preliminary conclusions will be drawn from them.

2. The Gradient Square Tensor

The GST has been proposed by Haglund [2] to estimate the local dimensionality. Van Vliet [3] presented a closed-form analytical solution in 2-D and applied it to estimate local orientation and anisotropy in geological data. Here we present a closed-form analytical solution for the eigenvalues and eigenvectors of the 3-D tensor which is defined by

$$GST = \overline{\mathbf{G}} = \overline{\mathbf{g} \bullet \mathbf{g}^{\mathbf{T}}} = \begin{pmatrix} \overline{g_x^2} & \overline{g_x g_y} & \overline{g_x g_z} \\ \overline{g_x g_y} & \overline{g_y^2} & \overline{g_y g_z} \\ \overline{g_x g_z} & \overline{g_y g_z} & \overline{g_z^2} \end{pmatrix} \qquad (1)$$

with **g** the gradient, which we compute with Gaussian derivatives of size $\sigma_{\mathrm{gradient}}$ and ($\overline{}$) a local smoothing operation (Gaussian of size σ_{tensor}).

This Gaussian filter can be extremely large. To speed up calculations we apply a recursive Gaussian filter [4]. The eigenvectors $\mathbf{v}_i$ with eigenvalues λ_i (i = 1, 2, 3) of a matrix **A** are defined by:

$$\mathbf{A} \bullet \mathbf{v}_i = \lambda_i \mathbf{v}_i \qquad (2)$$

The eigenvalues can be found by solving

$$\left| \overline{\mathbf{G}} - \lambda \mathbf{I} \right| = 0 \qquad (3)$$

This leads to solving a cubic equation of the form:

$$x^3 + a x^2 + b x + c = 0 \qquad (4)$$

with

$$\begin{aligned} a &= -\left(\overline{g_x^2} + \overline{g_y^2} + \overline{g_z^2} \right) = -trace(GST), \\ b &= \overline{g_x^2} \cdot \overline{g_y^2} + \overline{g_x^2} \cdot \overline{g_z^2} + \overline{g_y^2} \cdot \overline{g_z^2} - \overline{g_x g_y}^2 \\ &\quad - \overline{g_x g_z}^2 - \overline{g_y g_z}^2 \\ c &= \overline{g_z^2} \cdot \overline{g_x g_y}^2 + \overline{g_y^2} \cdot \overline{g_x g_z}^2 + \overline{g_x^2} \cdot \overline{g_y g_z}^2 \\ &\quad - \overline{g_x^2} \cdot \overline{g_y^2} \cdot \overline{g_z^2} - 2 \overline{g_x g_y} \cdot \overline{g_x g_z} \cdot \overline{g_y g_z} \end{aligned} \qquad (5)$$

The roots of this equation are the eigenvalues. Since we only have real coefficients *a*, *b* and *c* we can calculate the three roots analytically [5]:

$$\begin{aligned} x_1 &= -2\sqrt{Q} \cos\left(\frac{\Theta}{3} \right) - \frac{a}{3} \\ x_2 &= -2\sqrt{Q} \cos\left(\frac{\Theta + 2\pi}{3} \right) - \frac{a}{3} \\ x_3 &= -2\sqrt{Q} \cos\left(\frac{\Theta - 2\pi}{3} \right) - \frac{a}{3} \end{aligned} \qquad (6)$$

with

$$\Theta = \arccos\left(\frac{R}{\sqrt{Q^3}} \right) \qquad Q = \frac{a^2 - 3b}{9} \qquad R = \frac{2a^3 - 9ab + 27c}{54} \qquad (7)$$

The possible solutions of these roots can be visualised in complex space by the real values (because of the cosine) of the edges of three pieces of a six-piece pie (Figure 3:). The pie is a unit circle translated by $-a/3$ and scaled by $2\sqrt{Q}$. Because $0 \le \Theta \le \pi$ we can clearly see from Figure 3: that the following ordering is always true:

$$x_1 \le x_3 \le x_2 \qquad (8)$$

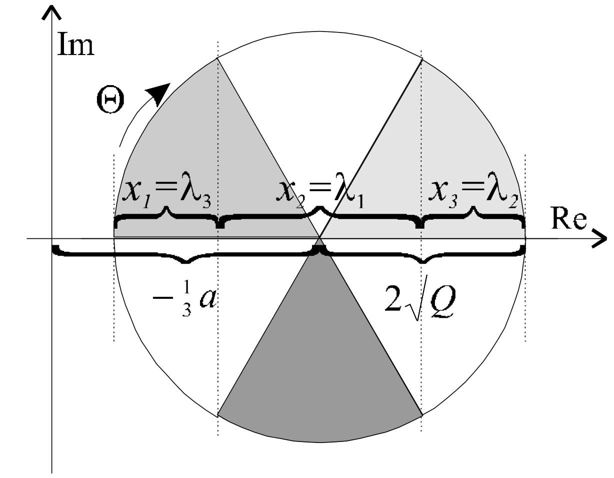

Figure 3: The ordering of the roots of the cubic equation becomes evident if depicted as the real values of the possible Θ. Θ increases in the direction indicated.

2.1 The 3D eigenvectors

With the eigenvalues found, we can now calculate the corresponding eigenvectors by using equation (2). Suppose we have an eigenvector with u_i, v_i and w_i its projections along the *x*-, *y*- and *z*-axis respectively, and eigenvalue (length) λ_i. We then need to solve the following equation:

$$\begin{pmatrix} \overline{g_x^2} - \lambda_i & \overline{g_x g_y} & \overline{g_x g_z} \\ \overline{g_x g_y} & \overline{g_y^2} - \lambda_i & \overline{g_y g_z} \\ \overline{g_x g_z} & \overline{g_y g_z} & \overline{g_z^2} - \lambda_i \end{pmatrix} \begin{pmatrix} u_i \\ v_i \\ w_i \end{pmatrix} = 0 \qquad (9)$$

which results in these three equations for u_i, v_i and w_i:

$$\begin{aligned} \vec{u}_i &= \frac{\vec{v}_i \cdot \overline{g_x g_y} + \vec{w}_i \cdot \overline{g_x g_z}}{\lambda_i - \overline{g_x^2}} \\ \vec{v}_i &= \frac{\vec{u}_i \cdot \overline{g_x g_y} + \vec{w}_i \cdot \overline{g_y g_z}}{\lambda_i - \overline{g_y^2}} \\ \vec{w}_i &= \frac{\vec{u}_i \cdot \overline{g_x g_z} + \vec{v}_i \cdot \overline{g_y g_z}}{\lambda_i - \overline{g_z^2}} \end{aligned} \qquad (10)$$

With these equations it is clear that the projections are linear dependent of each other. This dependence is not a problem when we realise that we only need the ratios of the projections in order to calculate the angles. In this case:

$$\begin{aligned} \varphi_i &= \arctan\left(\frac{u_i}{v_i}\right) \\ \theta_i &= \arccos\left(\left(\frac{u_i}{w_i}\right)^2 + \left(\frac{v_i}{w_i}\right)^2 + 1\right)^{-\frac{1}{2}} \end{aligned} \qquad (11)$$

with standard spherical coordinates *r*, φ and θ with *r*=1.

Because we are working with the squared tensor, we must be able to uniquely represent only half of the sphere. The other half can not be distinguished from the first. We choose to be able to represent the half enclosed by octant I, II, III and IV, as defined in Figure 4: . As we can see in Table 1 if we use only φ (the ratio between u and v) we can not distinguish between octant I and IV (nor VI and VII but those are outside the half-sphere).

So we must use the θ to distinguish between those octants. But equation (11) squares the ratios u/v and v/w, and thus cannot distinguish between the two octants either. We must therefore use an additional requisite:

$$\theta_i = \pi - \theta_i \qquad , \forall \frac{v}{w} < 0 \qquad (12)$$

Table 1: Determining the uniqueness of each vector using the signs of its projections and the signs of their ratios to determine the octant it is represented in.

u_i	v_i	w_i	octant	u_i/v_i	u_i/w_i	v_i/w_i
+	+	+	I	+	+	+
-	+	+	II	-	+	-
-	+	-	III	-	-	+
+	+	-	IV	+	-	-
+	-	+	V	-	-	+
-	-	+	VI	+	-	-
-	-	-	VII	+	+	+
+	-	-	VIII	-	+	-

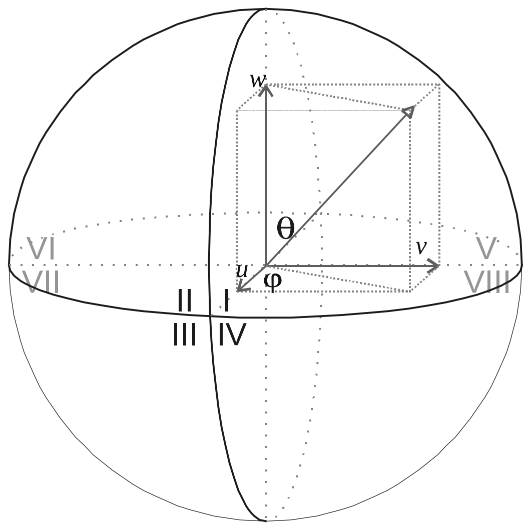

Figure 4: The sphere determining the total domain of possible eigenvectors, with definitions of the symbols used. It is divided into octants numbered I through VIII.

We can now fully distinguish any vector within the front half of the sphere in Figure 4: by the three variables λ_i, φ_i and θ_i. The domains of φ_i and θ_i are respectively [-½π, ½π] and [0, π]. Combining formulas (10), (11) and (12) results in the following analytical solutions for the angles of the eigenvectors:

$$\tan\varphi_i = \frac{\overline{g_x g_y}\left(\lambda_i - \overline{g_z^2}\right) + \overline{g_x g_z}\cdot\overline{g_y g_z}}{\overline{g_x^2}\cdot\overline{g_y^2} - \overline{g_x g_z}^2 - \lambda_i\left(\overline{g_x^2} + \overline{g_z^2}\right) + \lambda_i^2}$$

$$\cos\theta_i = \operatorname{sgn}\frac{v_i}{w_i}\times$$

$$\left(1 + \frac{\left(\overline{g_x g_y}\cdot\overline{g_x g_z} + \overline{g_y g_z}\left(\lambda_i - \overline{g_x^2}\right)\right)^2}{\left(\overline{g_x g_y}^2 - \left(\lambda_i - \overline{g_x^2}\right)\left(\lambda_i - \overline{g_y^2}\right)\right)^2} + \frac{\left(\overline{g_x g_y}\cdot\overline{g_y g_z} + \overline{g_x g_z}\left(\lambda_i - \overline{g_y^2}\right)\right)^2}{\left(\overline{g_x g_y}^2 - \left(\lambda_i - \overline{g_x^2}\right)\left(\lambda_i - \overline{g_y^2}\right)\right)^2}\right)^{-\frac{1}{2}} \quad (13)$$

3. Dimensionality Measures

The use of the GST can be demonstrated by looking at the result for three typical shapes: an edge or plane, a line or cylinder and noise. In Figure 5: the ellipsoid spaces spanned by the eigenvectors have been displayed in dark grey. These have been overlaid on the original grey object. The ratios of the sizes of the eigenvectors are representative for the dimensionality within the smoothing window. The absolute size of each vector is representative for the strength of the gradient in that direction. In an image with a reasonable SNR the sum of the eigenvectors will be quite low at regions dominated by noise. Areas in the image where the signal and orientation are strong will consequently have a larger sum of eigenvectors.

Table 2: Defining a measure of the local dimensionality dependent on the ratios of eigenvalues of the 3-D GST.

Dimensionality	relative eigenvalue sizes	Measure
Cylindrical (1D)	$\lambda_1 \approx \lambda_2 >> \lambda_3$	$\frac{\lambda_2 - \lambda_3}{\lambda_2 + \lambda_3}$
Planar (2D)	$\lambda_1 >> \lambda_2 \approx \lambda_3$	$\frac{\lambda_1 - \lambda_2}{\lambda_1 + \lambda_2}$
Isotrope (3D)	$\lambda_1 \approx \lambda_2 \approx \lambda_3$	$\sqrt{\lambda_1 + \lambda_2 + \lambda_3}$

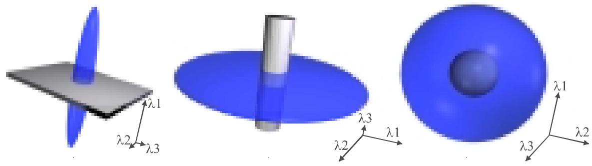

Figure 5: Visual representation of the ellipsoid space spanned by the eigenvectors of the Gradient Square Tensor resulting from the grey objects: a plane (a), a cylinder (b) and a sphere or isotropy (c).

Van Vliet [2] defined $1-\lambda_2/\lambda_1$ as a measure for anisotropy in 2D. We have translated this measure for the local dimensionality in 3D using three measures (Table 2). The planar and cylindrical measures are dimensionless so only the third measure, $\sqrt{\lambda_1 + \lambda_2 + \lambda_3}$, contains information about the strength of the gradient. This can be useful for separating noise from spherical objects, for example. Spherical objects will in general have a stronger gradient and therefore a larger eigenvalue than noise does.

4. Test results

Before applying the orientation tensor to three-dimensional CSLM images we need to validate the GST on test images for which the ground truth is known. Another important aspect is the robustness of the dimensionality measures in the presence of noise. We generated synthetic images of ellipsoids, cylinders and plane using analytical descriptions of their shapes. We use erfclipping [6] to ensure that generated images are approximately bandlimited.

To investigate the influence of noise on dimensionality detection, we take a look at several composite images. The original images were one of a cylinder through the centre and one of a plane. To these images various amounts of noise were added and the eigenvalues calculated. Instead of looking at the separate eigenvalues, we consider the dimensionality measures defined in the previous section. These measures determine the *x* and *y* position in the dimensionality image presented in Figure 6.

For visualisation purposes we have ignored the third - or 3D - axis. The value - or intensity - of each pixel is average amount of energy in the original image with the dimensionality indicated by the *x* and *y* position. The dimensionality image is displayed on a logarithmic intensity scale.

The dimensionality image is a composite image which means that the result from the planar and cylindrical images were calculated separately and then added to form a single image.

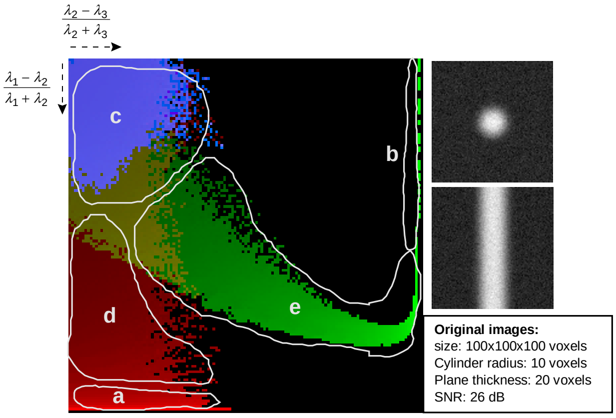

Figure 6: Composite image of a noisy plane, a noisy cylinder and pure noise calculated separately. It is clear that with an SNR of 26 dB the three dimensionalities are very well separated in the dimensionality space. (a) planar area, (b) cylindrical area, (c) isotropic area, (d) planar noise trail, (e) cylindrical noise trail.

For completeness' sake the dimensionality results from a realisation of noise with the same variance as the noise added to the objects has been displayed as well. We can roughly distinguish the following areas in the resulting images:

a) The area where the behaviour is distinctly planar. As the SNR decreases a trail develops towards the origin.
b) The area where the behaviour is cylindrical. The same as with the planar area, a trail towards the noisy area results from a decreased SNR.
c) The area where the behaviour is that of isotropy. Here all three eigenvalues are of about equal size. If the third measure had been taken into account, the absolute size of λ_1 in the *z*-direction, spherical objects and noise would have been separated in the *z*-direction but now they are both in this area of the image.
d) This is the trail developing from the noise of the planar image.
e) This trail develops from the cylindrical image as the SNR decreases. It does not lead directly to the area of isotropy. At a larger distance from the cylinder, the curvature of the cylinder becomes larger and resembles more and more a planar structure. Therefore the trail first moves towards the planar area before the signal becomes too weak and the trail moves totally towards the isotropic area.

When we look at a series of dimensionality images with decreasing SNR (Figure 7), we see that both the planar and the cylindrical areas move away from the border, the 'perfect' planar or cylindrical dimensionality, as the SNR worsens and leave a totally blank area.

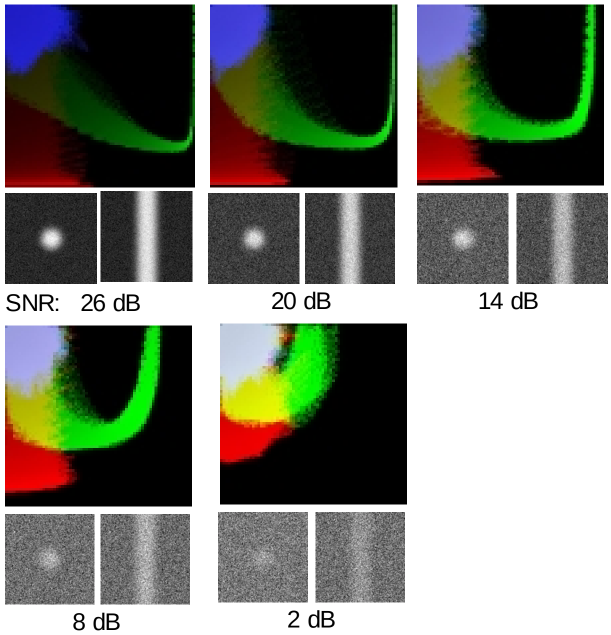

Figure 7: Series of dimensionality images with decreasing SNR. All images were calculated using the following Gaussian filter parameters: $\sigma_{gradient}$=1.5 and σ_{tensor}=5.

5. Confocal Image Formation

Confocal fluorescence microscopy provides a means of acquiring three-dimensional images of the microscopic network structure of gel-like food products (monoglycerides). Stained with Nile Red, the lipid network structure of these products can be made visible using fluorescence microscopy (see Figure 8).

Reliable and accurate measurements, however, require an optimised image formation that minimises the distortions imposed on the image by the image formation. Various distortions can hamper the data. Mismatches in refractive index between the immersion medium (the medium between the objective and coverslip) and the sample imposes a translation variant blurring on the image [7]. Scatter and reabsorption impose an attenuation of the fluorescence light intensity emitted from deeper layers in the sample.

In the following sections we address these distortions. The Nile Red dye concentration is optimised to minimise attenuation and improve the depth penetration in stained monoglycerides. We have applied attenuation correction software to the acquired images and show that this results in a further reduction of the attenuation of the pixel intensities at deeper layers in the image. Finally, image restoration is used to invert the blurring imposed by the confocal microscope.

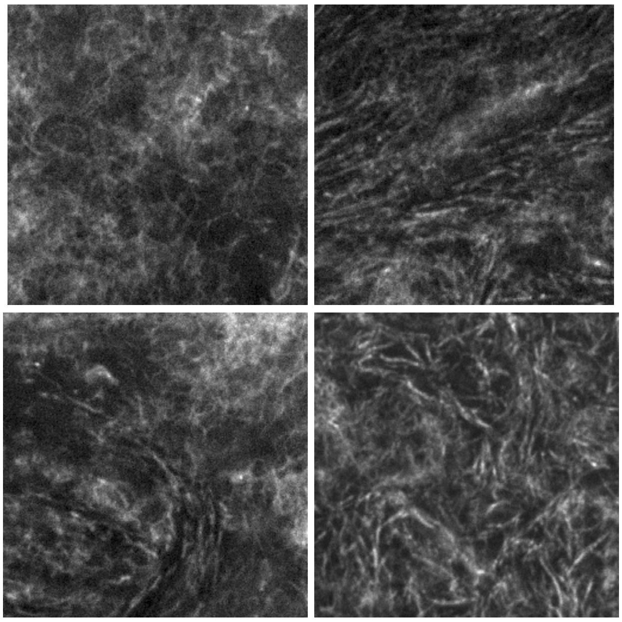

Figure 8: Representative lateral slices from 3-D images of four different monoglyceride systems.

5.1 Attenuation Reduction

Scatter and the absorption of the excitation light in higher layers will reduce the amount of light penetrating to deeper layers in the sample, attenuating the fluorescence light of these layers. The non-transparency of monoglycerides gives rise to scatter that attenuates the excitation light focussed on deeper layers of the sample. The amount of scatter is specific to the sample, and is unavoidable.

Another source of attenuation, the absorption of the excitation light and the re-absorption of the emitted light can be minimised by tuning the amount of the fluorescence dye the sample is stained with. We have investigated whether a reduction in the concentration of the Nile Red, used to stain the monoglyceride, reduces the attenuation. The monoglycerides are stained by means of diffusion. After a monoglyceride sample is put on a microscope glas, a glass filter (disk of porous glass) is placed on top of it. A drop of the stain is dropped on the filter. The filter slowly releases the fluorescent dye to the monoglyceride, which is then stained by diffusion. After an adequate staining of the sample, the filter is removed, and a glass cover in put over it to prevent it from drying up.

The mean intensity of a 5% monoglyceride sample (made in a beaker) is shown in Figure 9 as a function of depth for four different Nile Red concentrations (100%, 50%, 25% and 10%). The 100% concentration corresponds to 0.1 mg Nile Red per 1 ml of solvent (50 % polyethylene glycol, 45% glycerol, and 5% water). The figure clearly shows that the drop in intensity as a function of depth is less significant for lower concentrations. Therefore the attenuation caused by absorption is minimised with the use of a low concentration (10%) of the Nile Red fluorescence stain. We found that the use of an even lower concentration (2%) significantly reduces the fluorescence signal. We had to use a 30% laser power in this case instead of the 5-10% laser power used normally. We therefore conclude that for the investigated monoglyceride systems an optimal reduction of absorption induced attenuation is obtained with a Nile Red concentration of about 0.01 mg/ml. Furthermore, the reduction in stain concentration enable us to penetrate deeper in the sample (~15 µm for 100%, > 27 µm for 10%).

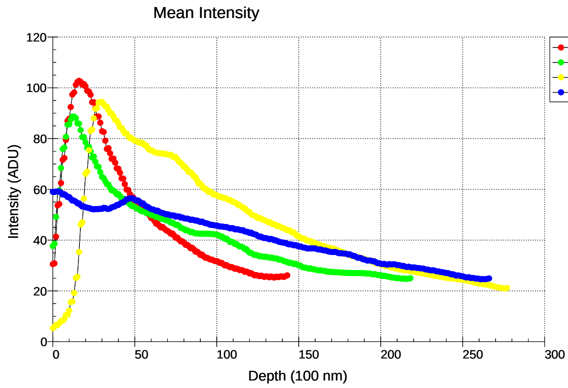

Figure 9: The mean intensity of 5% monoglyceride system as function of depth, stained with four different concentration of Nile Red. The 100% concentration corresponds to 0.1 mg/ml.

Attenuation can also be corrected for after acquisition. We have implemented the RAC-LT2 attenuation correction algorithm proposed by Strasters [8] and applied it to the monoglyceride images. The algorithm is based on the premise that the amount of local attenuation can be estimated from the amount of local fluophores. This is a reasonable model for both scatter- and absorption-induced attenuation. The intensity of a pixel is corrected by dividing it by a weighted sum of the acquired intensities in the light cone of the pixel being corrected. The weight, named the extinction coefficient, has to be estimated. Strasters applied his attenuation correction to images of individual cells. Therefore he could estimate the extinction coefficient by reasoning that the background intensity just above and just below a cell should be equal after correction. In our situation we cannot use this approach. Instead we reasoned that the monoglyceride images represent a large network structure of which the mean intensity should be constant. We have therefore estimated the extinction coefficient in such a way that after correction the mean intensity would remain constant as function of depth.

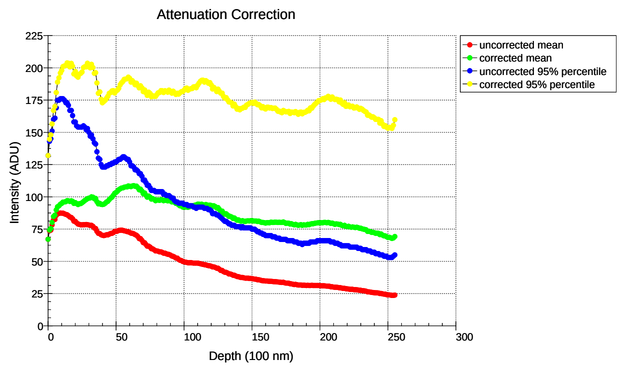

Figure 10: The mean intensity and the 95% percentile of the intensity distribution of a 25% stained monoglyceride as function of depth.

Figure 10 shows the result of applying the attenuation correction software to a 25% stained monoglyceride. It clearly shows that the decrease of the mean intensity as a function of depth is significantly reduced (we used an extinction coefficient of 0.006). To check that the procedure did not produce large intensity peaks, we also include the 95% percentile value of the intensity as a function of depth. Again this shows a proper correction.

5.2 Image Restoration

The 3-D confocal optical transfer function has an axial cut-off frequency that is about three times smaller than the lateral cut-off frequency [9]. This results in an anisotropic blurring of confocal images by the confocal point spread function. As a consequence, planar structures oriented laterally will be more blurred than axial oriented planes. This will greatly influence the gradient-based GST. Lateral oriented planes will prove more difficult to detect than axial oriented ones. To overcome this problem we have applied image restoration to invert the blurring imposed by the confocal microscope. We have used the iterative constrained Tikhonov-Miller (ICTM) algorithm [10, 11] to restore the confocal data.

The confocal point spread function has been computed using a theoretical model of the microscopic image formation, which is based on vectorial diffraction theory [12]. This model takes important microscopic parameters such as the finite-size pinhole, high numerical apertures, and polarization effects into account; lens aberrations are not modeled. The regularization parameter has been estimated with the generalized cross-validation method [11]. Figure 11 shows two slices of a 3-D confocal image of a monoglyceride before and after applying the ICTM algorithm.

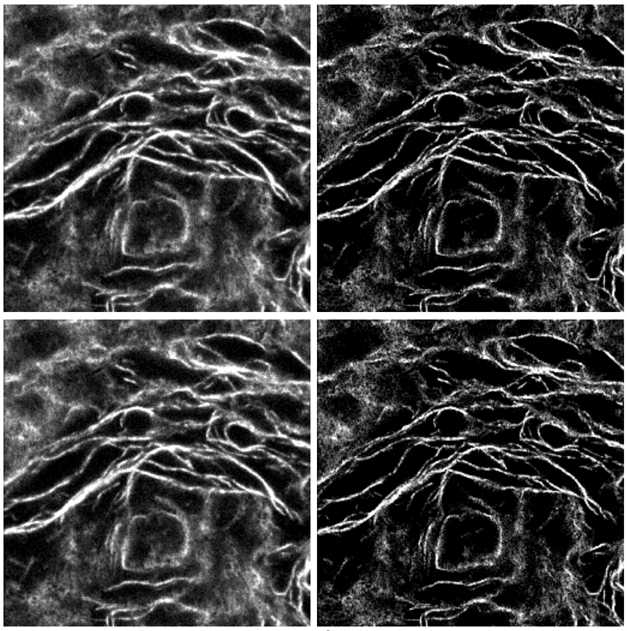

Figure 11: Two lateral slices of a 3-D monoglyceride image before (left) and after (right) applying image restoration.

5.3 Scale dependent Anisotropy Measurements

The analysis presented in this section, focuses on the dominant structure in the image as function of scale (σ_{tensor}). We have determined the average anisotropy at the various scales (see Figure 12) by computing the average over the image of

$$(\lambda_{12} - \lambda_3)/(\lambda_{12} + \lambda_3) \tag{14}$$

with λ_{12} the average of λ_1 and λ_2. This measure will produce values ranging from zero to one. A high value indicates an anisotropic structure, and low value indicates that the structure at the measured scale is isotropic. Using this measure we can distinguish between monoglycerides of various mass percentages and distinguish gels produced in a small votator with those produced in a beaker (see Figure 8).

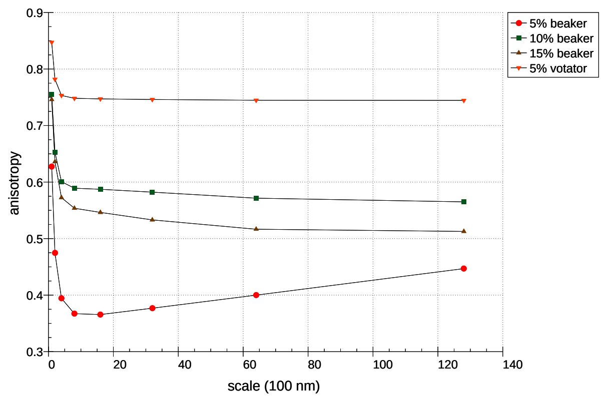

Figure 12: Scale dependent anisotropy measurements on various monoglycerides.

6. Discussion

This paper presents preliminary results of the application of the gradient square tensor (GST) to the analysis of 3-D microscopic network structures. We have derived closed-form expressions for the eigenvalues and eigenvectors of the 3-D smoothed gradient square tensor. The eigenvalues are used to determine the local dimensionality and the eigenvectors can be used to determine the corresponding orientation. Both the gradients and the smoothing of the GST are being computed using Gaussian convolution operations. This allows for both a classical scale-space approach by varying the scale of the gradient, as well as a "structure scale-space", determined by the amount of smoothing of the GST. Since the size of the smoothing kernels can become quite large, we have used a fast implementation of the Gaussian filter using recursive filters.

We have tested the proposed dimensionality measures of synthetic objects in the presence of noise. These tests show that planar, line and isotropic structures can be distinguished under realistic noise conditions.

A reliable application of the GST to confocal data, requires the confocal imaging to be optimised for quantitative analysis. We have used techniques to minimise the attenuation of the fluorescence intensity at greater depths and to improve the poor axial resolution by means of image restoration.

The analysis results on confocal images of monoglycerides show that the GST is a promising tool for a scale dependent analysis of the local dimensionality of network structures. We have demonstrated the use of the GST to measure the anisotropy of different microstructures. The analysis showed both a difference in anisotropy between different microstructures as well as their dependency as function of the structure scale.

Acknowledgements

We are grateful to R. van Adel for providing some of the confocal datasets. We like to thank dr. A. Sein for the intense discussions on the rheology and microstructure of monoglyceride systems. This work was partially supported by the Unilever Research Vlaardingen and the Delft University of Technology, by the Royal Netherlands Academy of Arts and Sciences (KNAW) and by the Rolling Grants program of the Foundation for Fundamental Research in Matter (FOM).

References

[1] I. Heertje, E.C. Roijers and H.A.C.M. Hendrickx, *Liquid Crystalline Phases in the Structuring of Food Products*, Lebensm.-Wiss. und Technol. 31, 1998, 387-396.

[2] L. Haglund, *Adaptive multi-dimensional filtering*, PhD Thesis, Linköking, 1992.

[3] Van Vliet, L.J. and Verbeek, P.W. *Estimators for orientation and anisotropy in digitized images.*, Proc. of First Annual Conference of the Advanced School for Computing and Imaging, ASCI, Delft, 1995, 442-450.

[4] L.J. van Vliet, I.T. Young, and P.W. Verbeek, *Recursive Gaussian Derivative Filters*, Proc. 14th Int. Conference on Pattern Recognition, IEEE Computer Society Press, Los Alamitos, 1998, 509-514.

[5] Press, W.H., Teukolsky, S.A., Vetterling, W.T. & Flannery, B.P. , *Numerical Recipes in C, 2nd edition.* Cambridge, Cambridge University Press, 1992.

[6] Van Vliet, L.J. *Grey-Scale Measurements in Multi-Dimensional Digitized Images.* Ph.D. thesis, Delft University of Technology, The Netherlands. 1993

[7] Hell S., Reiner, G., Cremer, C. & Stelzer, E.H.K. *Aberrations in confocal fluorescence microscopy induced by mismatches in refractive index*. J. of Microscopy 169, 1993, 391-405

[8] Strasters, K.C., Van der Voort, H.T.M., Geusebroek, J.M. & Smeulders, A.W.M. 1994 *Fast attenuation correction in fluorescence confocal imaging: a recursive approach.* BioImaging 2, 1994, 78-92.

[9] Wilson, T. & Tan, J.B. *Three dimensional image reconstruction in conventional and confocal microscopy*. BioImaging **1**, 1993, 176-184.

[10] van der Voort, H.T.M. & Strasters, K.C. *Restoration of confocal images for quantitative image analysis*. Journal of Microscopy **178**, 1995, 165-181.

[11] Van Kempen, G.M.P., Van Vliet, L.J., Verveer, P.J. & Van der Voort, H.T.M. *A Quantitative Comparison of Image Restoration methods for confocal microscopy*. J. of Microscopy 185, 1997

[12] van der Voort, H.T.M. & Brakenhoff, G.J. *3-D image formation in high-aperture fluorescence confocal microscopy: a numerical analysis*. Journal of Microscopy **158**, 1990, 43-54.